



The influence of turbulence on the laminar-turbulent transition in the wind tunnel and during free flight

U. Deck¹ · W. Würz¹

Received: 17 February 2025 / Revised: 7 June 2025 / Accepted: 11 June 2025 / Published online: 2 July 2025
© The Author(s) 2025

Abstract

During active convection high inflow turbulence is present in the lower earth atmosphere. This is relevant for airfoils with long run of laminar boundary layer since inflow turbulence effects the transition process and location. Therefore, research on the turbulence influence is an important topic in the field of natural laminar flow airfoils during the last decades. Free flight measurements have been used along with intensive wind tunnel investigations to study this effect. Whereas the comparison of free flight measurement data and wind tunnel results is already challenging for steady inflow conditions it is even more complex for higher inflow turbulence. This is mainly caused by the different spectral amplitude distributions for the inflow fluctuations in wind tunnels and in free flight. In the earth atmosphere, large scale fluctuations are always coupled with small scale turbulences. In the wind tunnel the artificial reproduction of large scale fluctuations is difficult due to the geometrical restrictions. However, the present study aims to compare free flight and wind tunnel test results for different inflow turbulences levels using a method which takes the different spectral amplitude distributions into account. Hotwire measurement techniques are employed to measure the time dependent inflow turbulences together with surface mounted hot-film sensors, which are used to capture integral and spectral boundary layer quantities. The latter ones show a dominant Tollmien–Schlichting wave transition process in the wind tunnel and during free flight. Integral values are in good agreement for the suction side of the airfoil but show some systematic differences between wind tunnel and free flight measurements for the pressure side.

Keywords Laminar-to-turbulent transition · Inflow turbulence · Free flight measurements · Wind tunnel measurements

Abbreviations

A/D	Analog / digital	T_{film}	Hot-film operating temperature
CTA	Constant temperature anemometry	α_{probe}	Angle of attack at the probe location
$\Delta\Sigma$	Delta-sigma A/D-converter	Θ_{wire}	Installation angle of hot-wire
IAG	Institute of aerodynamics and gas dynamics	A	Hot-wire calibration constant
LWT	Laminar wind tunnel	B	Hot-wire calibration constant
NLF	Natural laminar flow	n	Hot-wire calibration constant
Tu	Turbulence intensity	C_0	Hot-wire temperature calibration constant
α	Angle of attack	C_1	Hot-wire temperature calibration constant
μ_{∞}	Dynamic viscosity	C_2	Hot-wire temperature calibration constant
ρ_{∞}	Air density	E_{xx}	Power density
U_{∞}	Inflow velocity	C	Constant of Pope model spectrum
T_{∞}	Static air temperature	c	Chord
T_{wire}	Hot-wire operating temperature	C_f	Skin friction coefficient
		Re	Reynolds number
		D_{wire}	Diameter of hot-wire
		DC	Top-of-bridge voltage
		STD	Standard deviation
		κ, ω	Wave number
		ε	Dissipation rate
		f	Physical frequency

✉ U. Deck
ulrich.deck@iag.uni-stuttgart.de

¹ Institute of Aerodynamics and Gas Dynamics (IAG),
University of Stuttgart, Pfaffenwaldring 21, 70569 Stuttgart,
Germany

F	Non-dimensional frequency
F_{noise}	Factor of electronic noise
n_{noise}	Exponent of electronic noise
M	Take-off weight
Re	Reynolds number
S	Wing area
$V_{\text{eff.}}$	Effective inflow velocity
$\text{Re}_{\text{eff.}}$	Effective inflow Reynolds number
$\tau_{\text{eff.}}$	Effective wall shear stress
$c_{f,\text{eff.}}$	Effective skin friction coefficient
x	Chord wise position
y	Span wise position
x_{probe}	X-coordinate of probe position
x_{CG}	X-coordinate of center of gravity

1 Introduction

Within the design process of natural laminar flow (NLF) airfoils, used for general aviation aircraft or wind turbines, the inflow conditions are usually assumed to be steady without any disturbances. Recent research has shown that this assumption is not correct for flights at lower altitude during active convection, in the so called convection mixed layer [1]. Next to convective motions also wind shear can lead to higher turbulence intensities [2]. Especially NLF airfoils lose performance in the presence of atmospheric turbulence [3, 4]. Following a classical Kolmogorov cascade [5] atmospheric turbulence leads to fluctuations in angle of attack and micro-scale turbulence at higher frequencies. Both is affecting the airfoil and overall aircraft performance resulting in variations of lift, fluctuation in the transition location and thereby increased drag, especially in the region of the laminar bucket [6]. It has been found that changes of angle of attack or stagnation pressure variations directly lead to a highly time-variable pressure distribution [7], which produces an unsteady boundary layer development resulting in significant shifts of transition location in stream wise direction [8]. Especially on the lower side of modern NLF airfoils where pressure gradients are close to a flat plate case, this effect is significant [9]. In-line with the basic ideas of boundary layer receptivity [10, 11] a quantitative link can be established between the disturbance level found in the convective atmosphere and the boundary layer response. Nevertheless, the underlying physics is extremely complex [11], ranging from transition by exponential modal TS-wave growth [28] for turbulence levels $Tu \leq 0.2\%$ to dominating streamwise streaks, for example, Klebanoff modes, for $Tu \geq 1\%$ [29]. Research on the influence of small-scale turbulence on the transition location in free flight and research on free stream turbulence in the wind tunnel, generated with active grids, shows that increasing turbulence indeed causes a remarkable upstream movement of the transition location [12]. Within

the course of such investigations a wide set of experimental techniques were used to measure the unsteady transition location. Besides microphone arrays [6] mainly hot-film sensors [9, 12], dedicated pressure sensors with high frequency resolution [13, 14] and piezo film arrays [15] are employed. Flight measurements to determine the turbulence intensity in the convective layer have been performed multiple times in the past [16]. Even measurement of atmospheric turbulence using sailplanes flying in different types of updrafts have been performed so far [17]. Such studies often used hotwire constant temperature anemometers (CTA) to measure turbulence intensity and spectral distributions of inflow disturbances [6, 9]. While there are a few detailed studies comparing the turbulence characteristics in wind tunnel and in free flight [18] available comparisons of the effect on boundary layer development and airfoil performance are still rare [12, 13]. Within the present investigation the impact of inflow turbulence is studied on a NLF airfoil which exhibits completely different pressure distributions on the suction and pressure side. Forced by the coupling between integral lift and flight speed for operational conditions a wide range of conditions is covered and examined in detail. Thereby, the aim is not only to document the turbulence effect itself, but also to establish a route for modeling the effect of the earth atmosphere in a wind tunnel.

2 Methods

For the present study, hot-wire and hot-film measurement techniques are used in free flight experiments and in the Laminar Wind Tunnel (LWT) to determine and compare the influence of higher inflow turbulences. Both measurement techniques have to be in-situ calibrated using reference quantities, such as inflow velocity, angle of attack, air temperature and humidity, which are captured with standard pressure sensor measurements. To ensure correct reference quantities a probe calibration of the flight system is carried out in the LWT and numerical simulations are employed to determine correction factors. Both is described in Deck [19].

2.1 Hot-wire turbulence measurement

A DANTEC 55P61 X-wire probe is operated with a custom made CTA-bridge to measure inflow velocity and angle of attack with a frequency resolution up to $f=5\text{kHz}$. For frequencies above $f=5\text{kHz}$ the electronic noise exceeds the fluctuation amplitude. Hot-wire voltage signals are recorded at a sample rate of $N_s=50\text{kS/s}$ per channel simultaneously together with the hot-film signals with a DILIGENT MCC DT9857E $\Delta\Sigma$ -A/D converter. Reference quantities are recorded with a standard NI-USB 6218 A/D-converter at a sample rate of $N_s=10\text{kS/s}$ per channel. For the present study

all data is split into small blocks of $t=0.01s$, assuming constant inflow parameters for each block. In post-processing averaged values as well as spectra are computed for each block.

The calibration of the hot-wire sensors is carried out using a modified [20] King’s law [21] approach, which takes temperature changes during the free flight measurements into account.

$$DC^2 = (B \cdot Re_{eff}^n + A) \cdot (T_{wire} - T_{\infty}) \cdot C_0 \cdot (1 + C_1 \cdot T_{\infty} + C_2 \cdot T_{\infty}) \tag{1}$$

The calibration coefficient A , B and n as well as the hot-wire temperature T_{wire} are calculated for each flight. The hot-wire temperature changes slightly due to electrical resistances deviations in the supply wires for example, caused by different ambient temperatures. The constants $C_0=5.75e^{-5}$, $C_1=3.17e^{-3}$ and $C_2=-2.1e^{-6}$ are identical for all data sets. The effective Reynolds number is calculated with the following formula:

$$Re_{eff} = \frac{D_{wire} \cdot V_{eff} \cdot \rho_{\infty}}{\mu_{\infty}} \tag{2}$$

$$V_{eff} = U_{\infty} \cdot \cos(\Theta_{wire} - \alpha_{probe}) \tag{3}$$

Figure 1 illustrates the agreement between the fitted King’s law function and the measurement points for each measurement block.

For the wind tunnel measurements, a classical King’s law approach without the temperature correction could be used

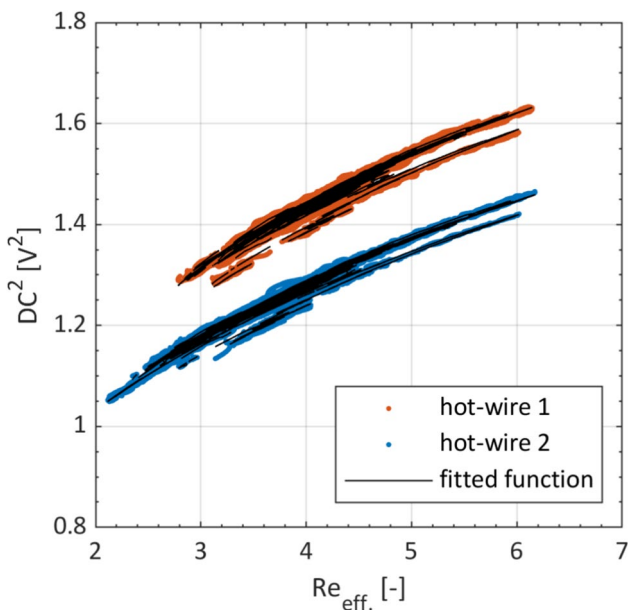


Fig. 1 Squared uncorrected DC voltage against effective Reynolds-number for both hot-wire sensors together with the fitted King’s law

since the temperature drift during one set of measurements has a negligible influence.

2.2 Hot-film boundary layer measurement

A similar approach is used to calibrate the hot-film sensors. Instead of the effective velocity the effective wall shear stress, normalized with the quotient of air density and viscosity is used as a reference quantity.

$$\tau_{eff} \cdot \frac{\rho_{\infty}}{\mu_{\infty}} = \frac{\rho_{\infty} \cdot U_{\infty}^2 \cdot c_{f,eff}}{2} \cdot \frac{\rho_{\infty}}{\mu_{\infty}} \tag{4}$$

The skin friction coefficient is calculated with XFOIL [22] for non-transitional boundary layer states related to the local lift coefficient. The boundary layer state is determined with the standard deviation of the hot-film voltage signal. A similar approach has been used by Seitz [23] (see Fig. 2). For the calibration the modified King’s Law formula now reads:

$$DC^2 = (B \cdot \tau_{eff}^n + A) \cdot (T_{film} - T_{\infty}) \cdot C_0 \cdot (1 + C_1 \cdot T_{\infty} + C_2 \cdot T_{\infty}) \tag{5}$$

In contrast to the hot-wire calibration, the hot-film calibration relies on one set of calibration coefficients, once calculated for a whole measurement campaign. This is acceptable since hot-film sensors show a better long time stability and additionally allows a more robust numerical calculation of the calibration.

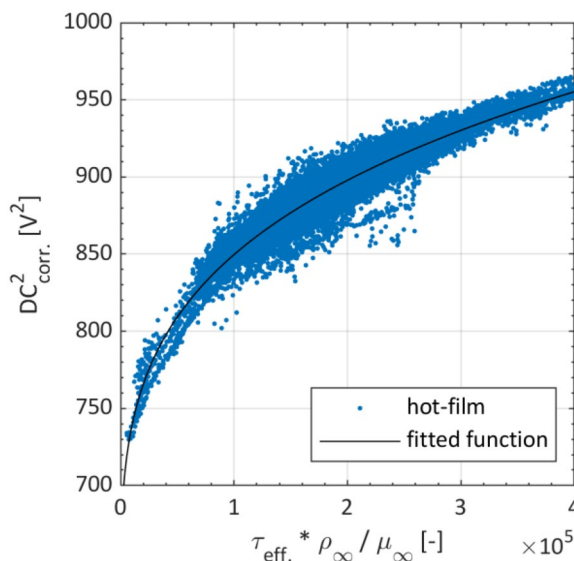


Fig. 2 Squared and temperature corrected DC voltage signal against effective wall shear stress for a hot-film sensor at $x/c=0.7$ on the suction side and the fitted King’s law

The calibration of the data sets from the LWT measurements is performed in a similar manner, but skipping the temperature correction akin to the hot-wire measurements.

2.3 Determination of dissipation rates

The dissipation rate ϵ defined by the Pope [24] model spectrum is used to quantify the turbulence level in this study.

$$E_{xx}(\kappa) = C \cdot \epsilon^{\frac{2}{3}} \cdot \kappa^{-\frac{5}{3}} \quad (6)$$

The model spectrum is fitted to power density spectra for the horizontal (E_{11}) and vertical (E_{22}) inflow velocity fluctuations, measured with the hot-wire probe. The power density spectra are calculated using the Welch's algorithm implemented in MATLAB R2022a for each $t=0.01$ s measurement block. Each spectrum is calculated with $N_S=1024$ spectral samples resulting in an overlapping of roughly 50% since each block contains only $N_S=500$ samples. A Hanning window is further applied to the spectral samples. Due to electronic noise, which covers the turbulence spectrum in the higher frequency regime, an additional term is added to the Pope model spectrum to enable the numerical fitting process.

$$E_{xx}(\kappa) = C \cdot \epsilon^{\frac{2}{3}} \cdot \kappa^{-\frac{5}{3}} + F_{\text{noise}} \cdot (2e^{-12} \cdot \kappa^{n_{\text{noise}}} + 1e^{-8}) \quad (7)$$

The variables F_{noise} and n_{noise} are further used to exclude measurement points with too high noise, which can also be caused by too high humidity leading to tiny droplets or due to pollen hitting the hot-wires [14].

The noise in the higher frequency regime is always more pronounced for the horizontal (E_{11}) fluctuations, see Fig. 3, since correlating disturbances are reduced for the vertical fluctuations (E_{22}) due to difference calculation of the hot-wire signals.

2.4 Free flight testing

Free flight tests have been carried out with the high-performance sailplane Ventus 3TS, manufactured by Schempp Hirth Segelflugzeugbau GmbH. The wing of this sailplane has a span of $b=18$ m and the wing area is $S=10,84$ m². The main airfoil of the wing is a natural laminar flow airfoil with laminar boundary layer flow up to $x/c=0.91$ on the pressure side and up to $x/c=0.7$ on the suction side. The airfoil is described in the following chapter. A custom made measurement system is mounted on the left wing at $Y=1980$ mm, refer to Fig. 4. Hot-wire probes are mounted together with a five-hole probe at $X=-1462$ mm on a boom in front of the wing. The hot-film sensor array is clued to the wing's surface at $Y=1630$ mm, further on a wake rake is placed at $Y=1378$ mm. The chord of the wing at the measurement

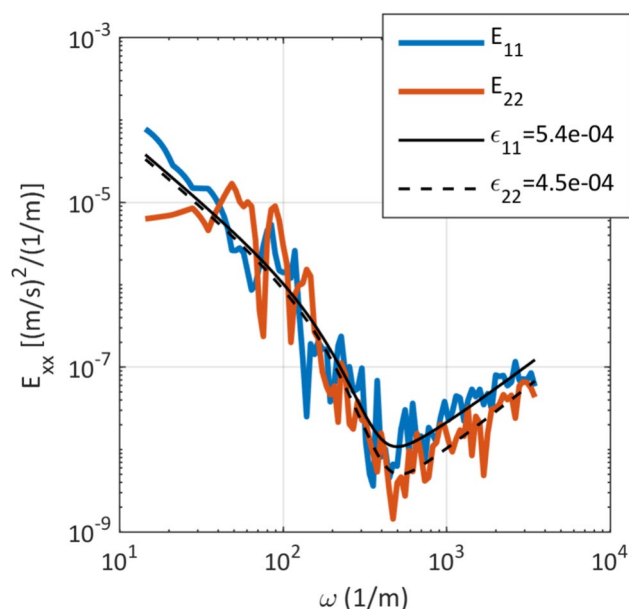


Fig. 3 Example power density spectrum for a $t=0.01$ s measurement block at $U_\infty=40$ m/s (colored lines) together with fitted Pope model spectrum (black lines)



Fig. 4 Test sailplane Ventus 3TS with mounted measurement system on the left wing during a test flight

section ($Y=1630$ mm) is $c=730$ mm. The box of the measurement system is streamlined to reduce the adverse influence of the measurement system itself. A detailed description of the measurement system is given in Deck [25].

In total, four measurement campaigns have been conducted with this measurement system. For the present study all data were collected in July 2021 during 14 flights with a total flight duration of $t=30$ h. The take-off weight during this measurement campaign was set to $M=449$ kg using removable water ballast. To capture different turbulence

conditions, flights early in the morning, before the convection starts, are performed together with flights in the afternoon, during active convection. The procedure of the measurement flights is explained in Deck [19].

2.5 Wind tunnel measurements

Wind tunnel tests have been performed in the LWT of the Institute for Aerodynamics und Gas Dynamics at the University of Stuttgart. A model of the WW14k130 main wing airfoil is used with the identical ($c = 730\text{mm}$) chord to achieve similar physical inflow velocities. The LWT itself is run with variable inflow velocity to reach an identical relationship between Reynolds number and lift coefficient compared to the free flight.

$$\text{Re}\sqrt{C_l} = \text{const.} = 1212747 \quad (8)$$

The wind tunnel model is equipped with the identical hot-film sensors at the same chord-wise position, additionally a wake rake is used for drag coefficient measurements downstream of the airfoil and pressure tubes to capture the airfoil pressure distribution (both not part of this study), see Fig. 5. The lift coefficient and angle of attack is measured with the standard LWT measurement system [26].

To investigate different inflow turbulence levels, the turbulence is artificially increased using passive grids in the settling chamber of the LWT. In total four different grids have been used. Two grids with only vertical elements, one with a rod diameter of $\varnothing = 32\text{mm}$ and a rod distance of $A = 200\text{mm}$ (D32A200) and another with a rod diameter of $\varnothing = 16\text{mm}$ and a rod distance of $A = 100\text{mm}$ (D16A100). Two further grids with vertical and horizontal elements, one with a rod diameter of $\varnothing = 5\text{mm}$ and a mesh size of

$M = 50\text{mm}$ (D5M50) and another with a rod diameter of $\varnothing = 2\text{mm}$ and a mesh size of $M = 20\text{mm}$ (D2M20). The spectral fluctuation characteristics of such passive grids have been investigated in detail by Romblad [18]. For the present study, hot-wire measurements have been performed using the same hot-wire probes, bridges and A/D converts as in the free flight measurements to determine the dissipation rates in the wind tunnel. Therefore, the hot-wire probe was mounted in the empty wind tunnel at the position of the leading edge with a boom of $L = 1\text{m}$ length.

The hot-film sensors, SENFLEX SF9902, have been applied on the wind tunnel model in the exactly same manner than on the Ventus 3TS wing surface. A thin adhesive tape is used, resulting in a total thickness of $60\mu\text{m}$. The free space between two sensors is filled using a foil which has the same thickness as the hot-film sensor to avoid any steps. The step at the edges of the sensor array is not smoothed out, since this was the most robust configuration during primary investigations in the wind tunnel concerning the transition location. Nevertheless, the transition location in the area of the hot-film array was carefully checked using a stethoscope before the final measurement for each grid configuration. No upstream shift of the transition location in the region of the hot-films compared to the clean airfoil was observed.

3 The WW14K130 airfoil

The main airfoil of the Ventus 3TS wing is the WW14k130 with relative thickness of $t = 13\%$ and a flap hinge at $x/c = 0.84$. During the present study the flap setting “WK-1” is investigated, which leads to a continuous pressure side without any kink at the flap hinge. The wind tunnel model has no deviations to the WW14k130 design geometry, whereas the actual airfoil on the wing slightly deviates from the design airfoil geometry (see Fig. 6). This leads to some geometrical deviations between the free flight airfoil contour and the wind tunnel airfoil.



Fig. 5 Test section of the LWT with the WW14k130 airfoil, hot-film sensors (brown stripes) applied in the upper part of the model

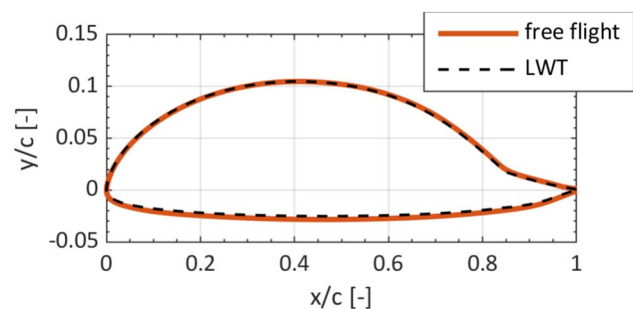


Fig. 6 Airfoil contour of the WW14k130

For both contours pressure distributions were calculated using XFOIL [22] to illustrate the impact of the geometrical deviations (see Fig. 7).

The differences in the pressure distribution are expected due to the geometrical deviations (Fig. 6). Nevertheless, the overall shape of the pressure distribution is nearly identical. On the pressure side, the pressure distribution is almost flat for all three angles of attack. In contrast, the pressure distribution on the suction side is curved showing a sharp adverse pressure gradient downstream of $x/c = 0.7$. On the pressure side the adverse pressure gradient starts at $x/c = 0.91$. Here, a bump tape is used just before the onset of the adverse pressure gradient to avoid any laminar separation bubble. This is not the case for the suction side. Therefore, a laminar separation bubble can be expected to show up on the suction side. This is already visible in the calculated pressure distributions. However, the design shape of the airfoil is trimmed to minimize the drag coefficient for the flight envelope, so the extend of the laminar separation bubble is just small enough to avoid any additional drag. For an angle of attack of $\alpha = 0^\circ$, there is a suction peak visible in the leading edge region of the pressure side. In contrast to the transition process on the suction side, this peak causes an immediately forward jumping transition front once the angle of attack falls below the critical value. This makes the transition location on the pressure side quite sensitive to large scale angle of attack fluctuations.

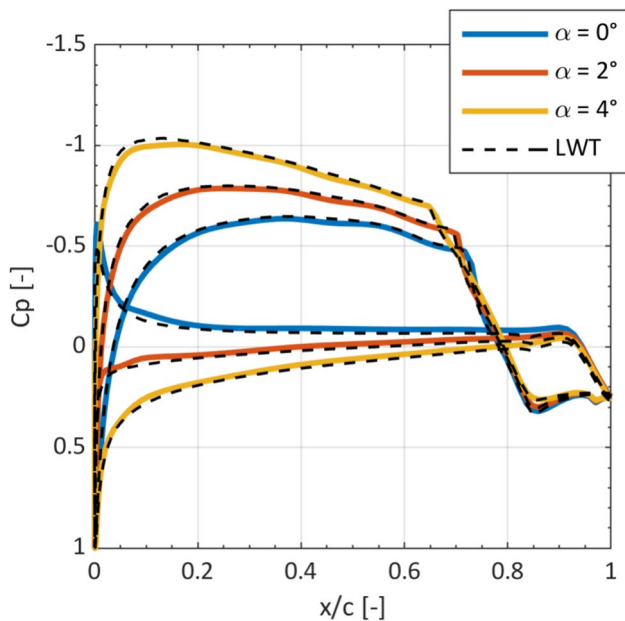


Fig. 7 XFOIL calculated pressure distributions for the free flight airfoil contour (colored lines) and for the WW14k130 design geometry used during the wind tunnel measurements (black lines)

4 Boundary conditions

For the comparison of free flight and wind tunnel measurements it is essential to ensure comparable inflow conditions. For incompressible cases with low turbulence intensity only two parameters, namely Reynolds number and angle of attack or lift coefficient, should be identical. This is challenging on its own since air temperature, humidity and static pressure are continuously changing during free flight tests, especially when using a sailplane since the flight altitude cannot be constant. But also the correct angle of attack or lift coefficient measurement is difficult since the flow field surrounding the test aircraft is three dimensional, whereas two dimensional flow conditions are usually realized in the wind tunnel. The most promising approach for lift coefficient measurement is the installation of several pressure tabs in the wing surface. This was not possible for this study due to the use of a rental test aircraft, which could not be modified. Therefore, a combined experimental and numerical approach was chosen to determine comparable lift coefficients and angles of attack. The measured values are corrected with the help of the numerical results to exclude deviations due to the flow field surrounding the test aircraft. Both is described together with a drag polar comparison in Deck [19].

When comparing free flight and wind tunnel data for higher turbulence intensities, there are two additional problems, which correlate. First of all, angle of attack fluctuations are always present during free flight measurements in a turbulent atmosphere [6], whereas, especially in the LWT, no noticeable angle of attack fluctuation is present even when using passive grids to increase the inflow turbulence. The second problem is the resulting spectral fluctuation amplitude distribution for artificial increased inflow turbulence in the LWT. Only for frequencies higher $f = 300\text{Hz}$ this distribution is comparable to spectra measured in the earth atmosphere [18]. Additionally, the relation between fluctuations in horizontal and vertical direction deviates in the wind tunnel from the behavior in the earth atmosphere, compare the dissipation rates (Fig. 8, blue lines) in the wind tunnel, which is caused by anisotropy due to the high contraction ratio of the LWT inlet section. For the present comparison of free flight and wind tunnel measurements the first problem is addressed using the unsteady angle of attack, measured at a frequency resolution of $f = 100\text{Hz}$ with the hot-wire probe, as a reference quantity. Since the angle of attack measured by the hot-wire probe drifts compared to the angle of attack measured by the pressure sensor based five-hole probe, an offset correction with a frequency resolution of $f = 1\text{Hz}$ for the hot-wire angle of attack measurement is applied. Further the angle of attack is measured in front of the

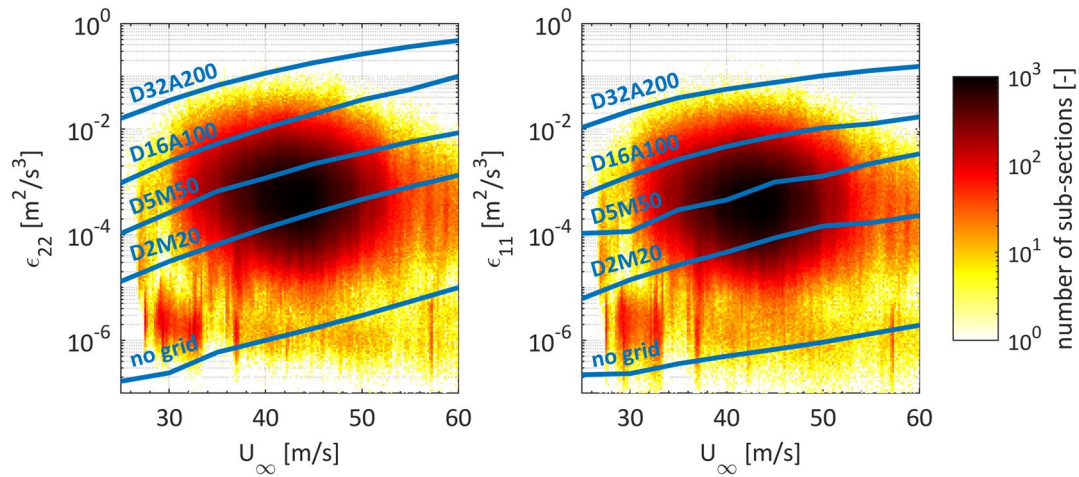


Fig. 8 2D histogram plot of free flight dissipation rates in terms of sub-section density for certain inflow velocities. Dissipation rates computed with the vertical inflow fluctuations in the left chart and

computed with the horizontal inflow fluctuations in the right chart. Dissipation rates obtained in the LWT for different passive grids in dependency of the inflow velocity are shown (blue lines)

wing, which causes an additional delay depending on the inflow velocity. With Δx being the distance between the measurement position of the angle of attack and the wing, this is compensated with the following formula:

$$t_{\text{delay}} = \frac{\Delta x}{U_{\infty}} \tag{9}$$

The high frequency resolution for the reference angle of attack is necessary since the transition location on the pressure side is influenced by a suction peak in the leading edge region, which reacts faster to an angle of attack fluctuation than the rest of the airfoil pressure distribution (see also chapter 3). Concerning the second issue related to the spectral fluctuation amplitude distribution it is obvious that the turbulence intensity as an integral value is not suitable as a reference quantity for the turbulence strength. Instead the Pope model spectrum [24] is fitted to spectra computed in short time intervals ($t=0.01s$), as explained in chapter 2.3. The short time intervals together with a Hanning windowing and detrending of the data sets before fast Fourier transformation, ensure that low frequency fluctuations, where wind tunnel and free flight fluctuation amplitudes deviate, are excluded. Resulting dissipation rates for free flight and wind tunnel measurement sub-sections are displayed in Fig. 8. Free flight dissipation rate distribution has the highest number of measurement sub-sections for a velocity of $U_{\infty} \approx 42m/s$ and a dissipation rate of $\epsilon \approx 5e-4m^2/s^3$. Of course, the distribution against velocity depends on the flight strategy during the measurements. Wind tunnel turbulence is increased using four passive grids, resulting in five discrete turbulence levels,

named as “turbulence categories” (“no grid”, “D2M20”, “D5M50”, “D16A100”, “D32A200”) in the following. For the most frequent free stream velocity of $U_{\infty} = 40m/s$ the turbulence quantities dissipation rate ϵ is given together with the well-known turbulence intensity Tu in Table 1 for each of these turbulence categories.

Corresponding dissipation rates (blue lines, Fig. 8) are then used to select free flight measurement sub-sections with similar dissipation rates, using a criterion for the velocity depending dissipation rates according to the following formula.

$$\epsilon_{LWT}(U_{\infty}) \cdot 0.9 < \epsilon_{\text{flight}}(U_{\infty}) < \epsilon_{LWT}(U_{\infty}) \cdot 1.1 \tag{10}$$

Resulting in a selection of free flight measurement sub-sections with comparable inflow turbulence to the wind tunnel turbulence categories. For the results discussed in chapter 5 the dissipation rates based on the vertical fluctuations (left chart of Fig. 8) are employed, because of their higher amplitudes in the wind tunnel.

Table 1 Turbulence quantities for $U_{\infty} = 40m/s$

	$\epsilon_{22,LWT}$	$Tu_{22,LWT,5Hz-3kHz}$	$\epsilon_{11,LWT}$	$Tu_{11,LWT,5Hz-3kHz}$
No grid	$1.0e^{-6}$	0.069%	$5.0e^{-7}$	0.026%
D2M20	$1.3e^{-4}$	0.35%	$4.7e^{-5}$	0.091%
D5M50	$1.2e^{-3}$	0.66%	$4.6e^{-4}$	0.22%
D16A100	$1.1e^{-2}$	1.07%	$4.7e^{-3}$	0.29%

5 Results

The measurement sub-sections of each inflow turbulence categories are selected from the free flight data sets to match with the dissipation rates in the LWT as described in chapter 4. All measurement sub-sections with identical angle of attack are averaged within each turbulence category using moving-mean and standard mean approaches in MATLAB.

5.1 Integral quantities

It is possible to distinguish laminar, turbulent and transitional boundary layer flows using the standard deviation of the hot-film voltage signals. The transition point is defined as the maximum of the standard deviation [27]. In this case, especially for the transition angle of attack, there is an offset between the transitions point in free flight and in the wind tunnel, for both sides of the airfoil, respectively. This is caused by difficulties in defining a proper reference angle of attack without offset mistakes due to the three dimensional flow state nearby the measurement box. Additionally,

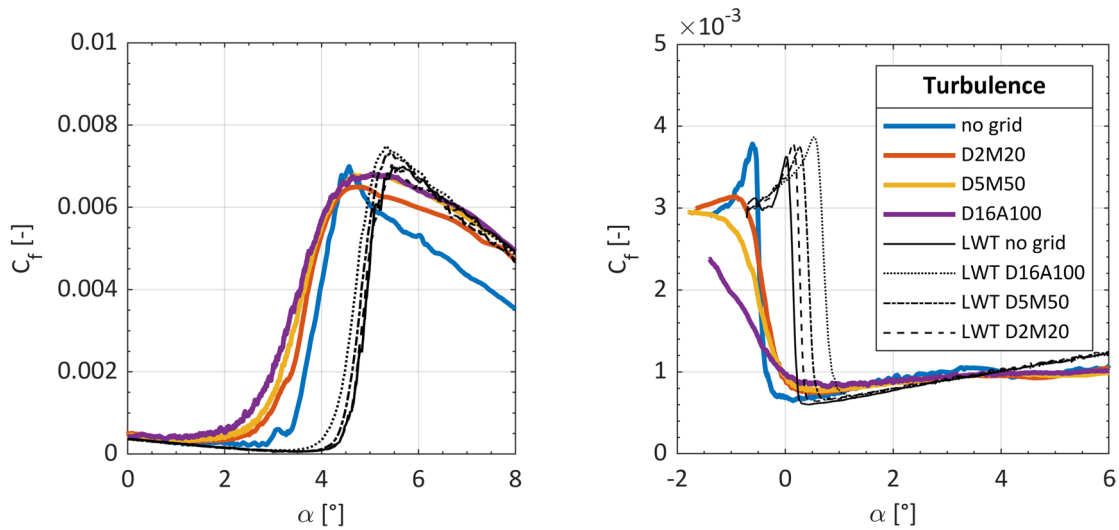


Fig. 9 Skin friction coefficient for a sensor location at $x/c=0.6$ on the suction side (left chart) and at $x/c=0.9$ on the pressure side (right chart). Results for different inflow turbulence in free flight and in the LWT are displayed

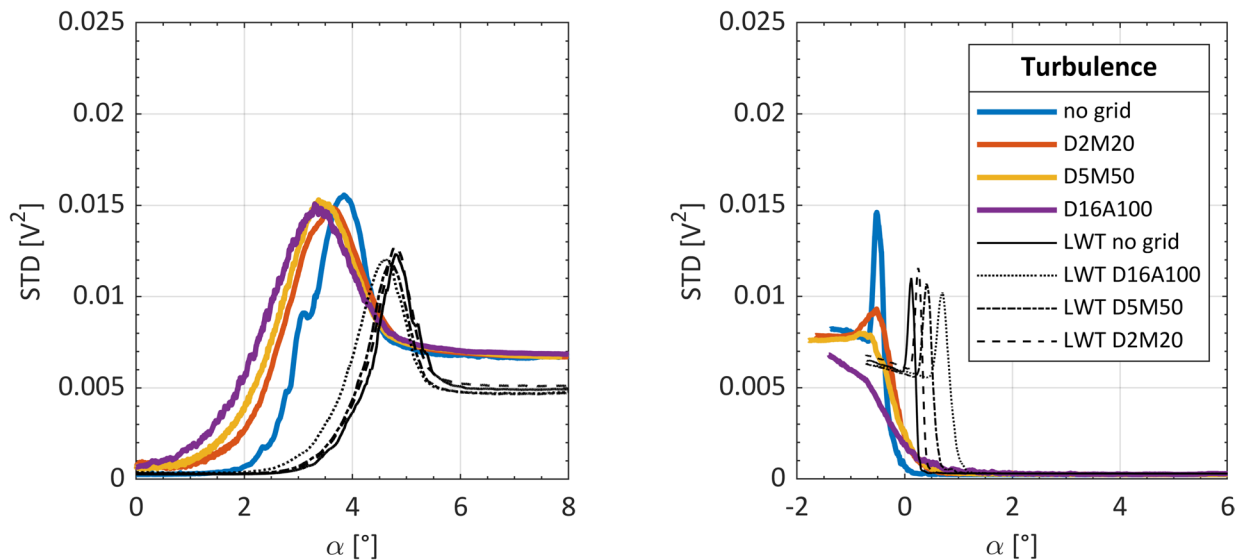


Fig. 10 Standard deviation of the hot-film voltage signal for a sensor location at $x/c=0.6$ on the suction side (right chart) and at $x/c=0.9$ on the pressure side (left chart). Results for different inflow turbulence in free flight and in the LWT

during free flight the flap angle deviates slightly due to structural deformations of the kinematic. However, for this study already the changes of the transition location for different inflow turbulence categories is sufficient. Together with the skin friction charts (Fig. 9), the standard deviation charts (Fig. 10) clearly illustrate a shift in the transition angle of attack due to higher inflow turbulence. For the suction side the transition angle of attack is reduced by roughly $\Delta\alpha=0.7^\circ$ when the inflow turbulence increases from the category “no grid” to “D16A100” in free flight and by roughly $\Delta\alpha=0.4^\circ$ in the LWT. The $\Delta\alpha$ deviation is in agreement with the expected behavior and confirms the applicability of the comparison method. For the pressure side no clear transition angle of attack displacement can be identified with the present method for the free flight test data. This is no opposition to the airfoil drag coefficient measurements, which show a significant additional drag at the lower corner of the laminar bucket, as presented in Deck [19]. Keeping in mind that drag coefficient measurements are conducted with an integration wake rake and thus low frequency resolution, whereas here the frequency resolution is $f=100\text{Hz}$. Therefore, low frequency angle-of-attack fluctuations are affecting the drag coefficient measurements, but not the presented hot-film measurements in this study. As mentioned in chapter 4 the idea behind the applied method is to exclude low-frequency angle-of-attack fluctuations from the present results as good as possible. This makes it possible to compare the results to the wind tunnel measurements, where no low-frequency angle-of-attack fluctuations are present. In the LWT, there is a significant increase in the transition angle of attack by $\Delta\alpha=0.8^\circ$, when increasing the turbulence from “no grid” to “D16A100”. Although it is not fully understood what causes

this difference between the free flight and the wind tunnel study, it is conspicuous that the measurements from Guissart [12] and Romblad [13] show the same difference for cases with a likewise pressure distribution of the regarded airfoil.

5.2 Spectral analysis

To investigate the transition process by spectra from the hot-film wall shear stress values, power spectral density is computed with the Welch’s algorithm, again for the measurement sub-sections with a duration of $t=0.01\text{s}$. To enable a comparison of spectra with different inflow conditions, such as air density and viscosity, the non-dimensional frequency parameter F is used instead of the physical frequency f in the charts [13].

$$F = \frac{2 \cdot \pi \cdot f \cdot \nu}{U_\infty^2} \tag{11}$$

This leads to a shift of the electronic noise floor of the spectra, which are dependent on the physical frequency (compare the left chart of Fig. 11, $F > 0.5 \times 10^{-4}$). The spectra are always computed and averaged for sub-sections having the same AOA.

To get comparable spectra with a similar boundary layer state, an offset angle of attack is introduced to compensate for the undesired offset between LWT and free flight results. This offset is determined from the results without any artificial turbulence in the LWT (turbulence category “no grid”). Due to the inflow velocity depended flap angle deviation and induced angle of attack the offset also depending on the

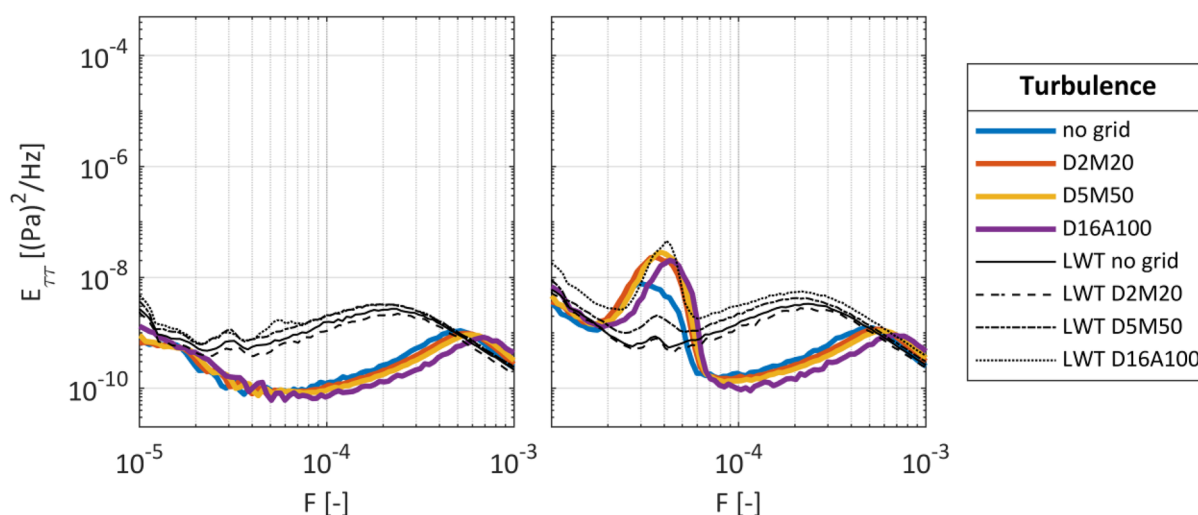


Fig. 11 Power density spectra of the wall shear stress for a hot-film location at $x/c=0.6$ (left diagram) and at $x/c=0.9$ (right diagram) on the pressure side for an angle of attack of $\alpha=0.31^\circ$. Spectra for differ-

ent inflow turbulences in free flight (colored lines) and in wind tunnel (black lines)

inflow velocity and thus on the mean angle of attack values, resulting in different values for each airfoil side.

$$\alpha_{\text{LWT, corr., suction side}} = \alpha_{\text{LWT}} - 0.96^\circ \quad (12)$$

$$\alpha_{\text{LWT, corr., pressure side}} = \alpha_{\text{LWT}} - 0.6^\circ \quad (13)$$

With this angle of attack offset it is now possible to compare the transition process. In Fig. 11, pressure side, there are for both, wind tunnel and free flight data sets, at $x/c=0.6$ for $\alpha=0.31^\circ$ no signs of a beginning transition process visible, whereas at $x/c=0.9$ higher amplitudes at $F \sim 4e^{-5}$ are visible, which is a sign for the involvement of Tollmien Schlichting (TS-) waves in the beginning transition process. For $\alpha=-0.47^\circ$ (Fig. 12) the agreement between free flight measurements and wind tunnel test is poor. At $x/c=0.6$ the transition process in the wind tunnel seems to be more evolved, at $x/c=0.9$ both data sets show the spectra of a fully turbulent boundary layer flow, for the free flight data at least for the “no grid” turbulence category. For the turbulence categories with higher inflow turbulence amplitudes are getting smaller at an angle of attack of $\alpha=-0.47^\circ$ (Fig. 12, right chart). This could be explained by a remaining influence of low frequency angle of attack fluctuations in free flight, which allow temporary a full laminar boundary layer flow, which is not the case in the wind tunnel.

For the suction side amplitude peaks match well between free flight data sets and corresponding wind tunnel measurements for the spectra at $x/c=0.6$ for $\alpha=2.06^\circ$ (Fig. 13, right chart), at $x/c=0.5$ and at $x/c=0.6$ for $\alpha=3.25^\circ$ (Fig. 14, left and right chart). Furthermore, overlaid scaled amplitudes of the TS-wave instabilities, calculated with LST (grey line),

show good agreement regarding the frequencies of the highest amplitudes. The applied LST method is based on integral boundary layer quantities, calculated with XFOIL [22]. Some difference is visible in the amplitude level between wind tunnel and free flight data with increasing turbulence, especially at $x/c=0.6$ for $\alpha=2.06^\circ$ (Fig. 13, right chart). Because of the fact, that there are no signs for TS-waves visible at $x/c=0.5$ for $\alpha=2.06^\circ$ (Fig. 13, left chart) only for the wind tunnel data set this indicates a further developed TS-wave transition process in the free flight data. In general, the overall agreement is quite good for the suction side, which shows accordance between the transition process in the wind tunnel and during free flight, even if the angle of attack fluctuation is only occurring in free flight.

6 Conclusion and outlook

In this study, a method to compare free flight and wind tunnel measurement results for higher inflow turbulences is presented. The method is based on a reference angle of attack with high frequency ($f=100\text{Hz}$) resolution for the free flight data, which is affected by strong angle of attack fluctuations. Further, it is essential to use dissipation rates, which are calculated by a fitted model spectrum to classify the inflow turbulence. The often used turbulence intensity is unsuitable, since it is an integral value and the spectral fluctuation amplitude distribution deviates between wind tunnel and the earth atmosphere for frequencies below $f=300\text{Hz}$.

To ensure the high frequency resolution simultaneously sampled hot-wire and hot-film probes have been used. Reference angle of attack and dissipation rates are measured

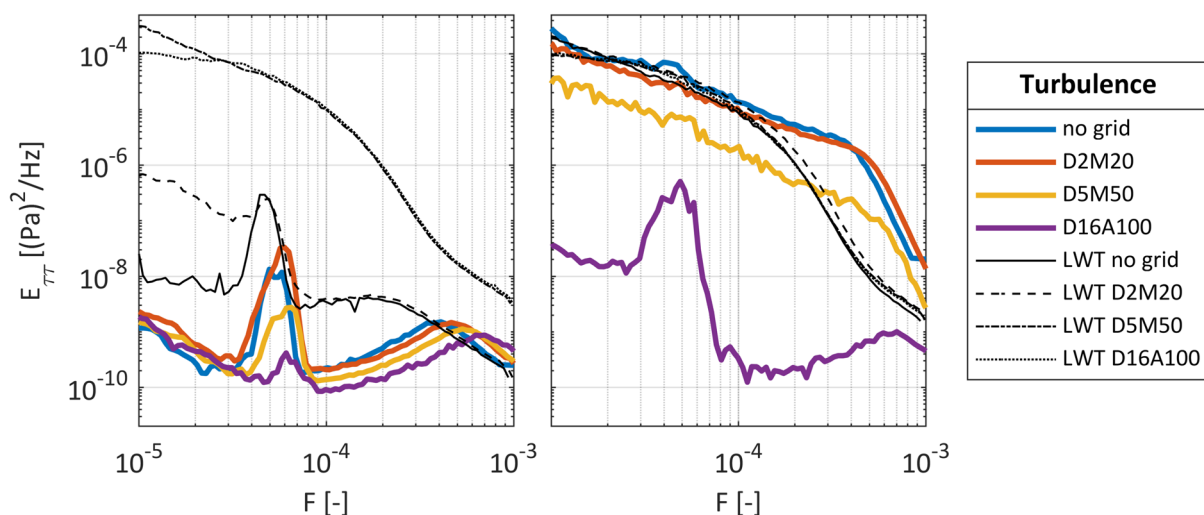


Fig. 12 Power density spectra of the wall shear stress for a hot-film location at $x/c=0.6$ (left diagram) and at $x/c=0.9$ (right diagram) on the pressure side and for an angle of attack of $\alpha=-0.47^\circ$. Spectra for

different inflow turbulence categories in free flight (colored lines) and in wind tunnel (black lines)

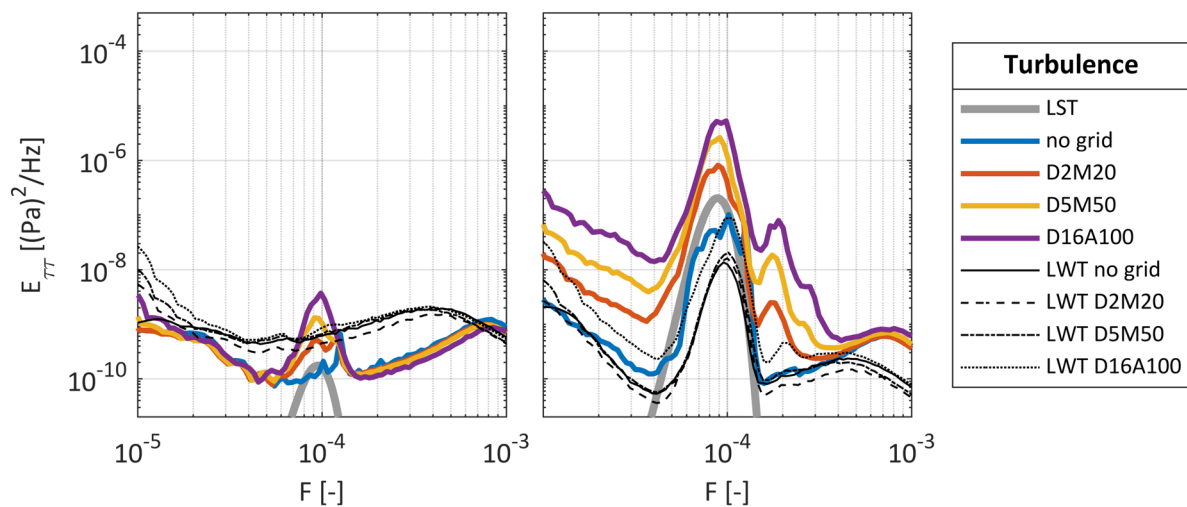


Fig. 13 Power density spectra of the wall shear stress for a hot-film location at $x/c=0.5$ (left diagram) and at $x/c=0.6$ (right diagram) on the suction side and for an angle of attack of $\alpha=2.05^\circ$. Spectra for

different inflow turbulence categories in free flight (colored lines) and in wind tunnel (black lines)

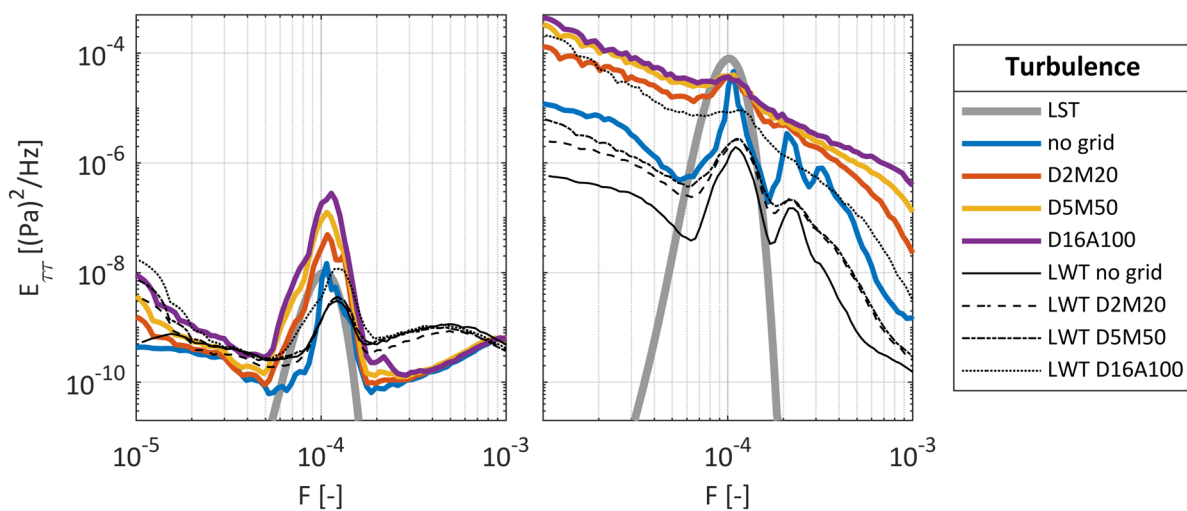


Fig. 14 Power density spectra of the wall shear stress for a hot-film location at $x/c=0.5$ (left diagram) and at $x/c=0.6$ (right diagram) on the suction side for an angle of attack of $\alpha=3.25^\circ$. Spectra for different inflow turbulences in free flight (colored lines) and in wind tunnel (black lines)

with a hot-wire probe. The hot-film data are used to quantify the laminar-to-turbulent boundary layer transition. For the suction side of the investigated airfoil there is good agreement between the wind tunnel study and the free flight tests. The shift of the transition location due to increased inflow turbulence, evaluated with the integral quantities standard deviation and skin friction coefficient, is comparable between wind tunnel and free flight measurements. Further on, the spectral investigation of the hot-film determined wall shear stress fluctuations unveiled a similar TS-wave driven transition process on the suction side. Both, frequency and amplitude excitation, are comparable between the data sets.

For the pressure side, which shows some similarities to a flat plat test case, the results obtained in free flight and in the wind tunnel deviate. However, the transition location in the wind tunnel shifts remarkably with increasing inflow turbulence. No such behavior could be shown for the free flight test results. One possible explanation for this distinguished behavior on the pressure side of the airfoil is its sensitivity to low frequency angle of attack fluctuations due to the suction peak in the leading edge area with a strong impact on the transition location. Nevertheless, the performed comparison also shows that determining comparable reference conditions is challenging, especially when no measurement of

the pressure distribution is possible. It is, therefore, recommended for future studies to use airfoil pressure distribution measurement techniques, even in free flight.

Acknowledgements The presented study is part of the LuFo-VI project “HPIA”, FKZ: 20Q1950B. This project was founded by the Federal Ministry of Economic Affairs and Climate Action (BMWK), based on a decision by the German Bundestag.

Author contributions U.D. wrote the main manuscript text and prepared all figures. W.W. reviewed the manuscript.

Funding Open Access funding enabled and organized by Projekt DEAL.

Data availability No datasets were generated or analysed during the current study.

Declarations

Conflict of interest The authors declare no competing interests.

Open Access This article is licensed under a Creative Commons Attribution 4.0 International License, which permits use, sharing, adaptation, distribution and reproduction in any medium or format, as long as you give appropriate credit to the original author(s) and the source, provide a link to the Creative Commons licence, and indicate if changes were made. The images or other third party material in this article are included in the article’s Creative Commons licence, unless indicated otherwise in a credit line to the material. If material is not included in the article’s Creative Commons licence and your intended use is not permitted by statutory regulation or exceeds the permitted use, you will need to obtain permission directly from the copyright holder. To view a copy of this licence, visit <http://creativecommons.org/licenses/by/4.0/>.

References

- Kaimal, J.C., Finnigan, J.J.: Atmospheric Boundary Layer Flows, Their Structure and Measurement. Oxford University Press, New York (1994). (ISBN 0-19-506239-6)
- Wyngaard, J.C.: Atmospheric turbulence. *Annu. Rev. Fluid Mech.* **24**(1), 205–234 (1992)
- Bertolotti, F.P.: Effect of atmospheric turbulence on a laminar boundary-layer. *Tech. Soar.* **25**, 154–159 (2001)
- Bernardy, S.: Investigation into the effects of turbulence in thermals on sailplane airfoil performance, Diploma Thesis, Delft University of Technology, Fachhochschule Aachen (2002)
- Kolmogorov, A.: The local structure of turbulence in incompressible viscous fluid for very large Reynolds numbers. *Cr Acad. Sci. URSS* **30**, 301–305 (1941)
- Weismüller, M.: A new approach to aerodynamic performance of aircraft under turbulent atmospheric conditions, Dissertation, Technische Universität Darmstadt, Deutschland (2011)
- Sears, W.R.: Some aspects of non-stationary airfoil theory and its practical application. *J. Aeronaut. Sci.* **8**(3), 104–108 (1941)
- Studer, G., et al.: Laminar-turbulent transition in oscillating boundary layer: experimental and numerical analysis using continuous wavelet transform. *Exp. Fluids* **41**, 685–698 (2006). <https://doi.org/10.1007/s00348-006-0190-01>
- Reeh, A.D.: Natural laminar flow airfoil behavior in cruise flight through atmospheric turbulence, Dissertation, Technische Universität Darmstadt (2014)
- Morkovin, M.V.: Critical evaluation of transition flow laminar to turbulent shear layers with emphasis of hypersonically traveling bodies, AFFDL TR, pp. 68–149 (1968)
- Saric, W., ReedKerschen, H.L.E.J.: Boundary-layer receptivity to freestream disturbances. *Annu. Rev. Fluid Mech.* **34**, 291–319 (2002)
- Guissart, A., Romblad, J., Nemitz, T., Tropea, C.: Small-scale atmospheric turbulence and its impact on laminar-to-turbulent transition. *AIAA J.* **59**(9), 3611–3621 (2021)
- Romblad, J.: Experiments on the laminar to turbulent transition at unsteady inflow conditions, Dissertation, Universität Stuttgart, Deutschland (2023)
- Greiner, M.: Experiments on laminar separation bubbles under inflow conditions of atmospheric turbulence, Dissertation, University of Stuttgart (2023)
- Peltzer, I.: Comparative in-flight and wind tunnel investigation of the development of natural and controlled disturbances in the laminar boundary layer of an airfoil. *Exp. Fluids* **44**, 961–972 (2008)
- Riedel, H., Sitzmann, M.: In-flight investigations of atmospheric turbulence. *Aerosp. Sci. Technol.* **2**, 301–319 (1988)
- MacCready, P.B.: Turbulence measurements by sail-plane. *J. Geophys. Res.* **67**, 1041–1050 (1962)
- Romblad, J., Greiner, M., Guissart, A., Würz, W.: Characterization of low levels of turbulence generated by grids in the settling chamber of a laminar wind tunnel Experiments in Fluids, pp. 63–65 2022
- Deck, U., Würz, W.: Freiflugmessungen der Profilpolare eines Laminarprofils unter konvektiven Anströmbedingungen, DLRK 2023, 19.09.-21.09., Stuttgart, 2023
- Hultmark, M., Smits, A.: Temperature corrections for constant temperature and constant current hot-wire anemometers. *Meas. Sci. Technol.* **21**(2010), 105404 (2010)
- Bruun, H.H.: Hot-Wire Anemometry, Principles and Signal Analysis. Oxford University Press, Oxford (1995)
- Drela, M.: XFOIL: an analysis and design system for low Reynolds number airfoils. In: Mueller, T.J. (ed.) Low Reynolds number Aerodynamics. Springer, Berlin Heidelberg (1989). https://doi.org/10.1007/978-3-642-84010-4_1
- Seitz, A.: Freiflug-Experimente zum Übergang laminar-turbulent in einer Tragflügelgrenzschicht, Dissertation, Institut für Aerodynamik und Strömungstechnik, Deutsches Zentrum für Luft- und Raumfahrt, Braunschweig, DLR-FB—2007-01, 2007
- Pope, S.B.: Turbulent Flows. Cambridge University Press, Cambridge (2000)
- Deck, U., Würz W.: In-flight measurements on the influence of freestream turbulence on a NLF airfoil, AIAA AVIATION 2023, San Diego, CA, AIAA 2023–3675 (2023)
- Althaus, D.: Measurement of lift and drag in the laminar wind tunnel, Institute report, IAG (2003)
- Kornberger, M.: Multisensor-Heißfilmetechnik zur Transitionserkennung im Windkanal- und Flugversuch, Fakultät für Maschinenwesen der Rheinisch-Westfälischen Technischen Hochschule Aachen, Dissertation (1992)
- Kachanov, Y.: Physical mechanisms of laminar-boundary layer transition. *Annu. Rev. Fluid Mech.* **26**, 411–482 (1994)
- Fransson, J.H.M., Shahinfar, S.: On the effect of free-stream turbulence on boundary-layer transition. *J. Fluid Mech.* **899**, A23 (2020)

Publisher’s Note Springer Nature remains neutral with regard to jurisdictional claims in published maps and institutional affiliations.